

Mosaic-Based Color-Transform Optimization for Lossy and Lossy-to-Lossless Compression of Pathology Whole-Slide Images

Miguel Hernández-Cabronero*, Victor Sanchez, *Member, IEEE*, Ian Blanes, *Senior Member, IEEE*, Francesc Aulí-Llinàs, *Senior Member, IEEE*, Michael W. Marcellin, *Fellow, IEEE*, and Joan Serra-Sagristà, *Senior Member, IEEE*.

Abstract—The use of whole-slide images (WSIs) in pathology entails stringent storage and transmission requirements because of their huge dimensions. Therefore, image compression is an essential tool to enable efficient access to these data. In particular, color transforms are needed to exploit the very high degree of inter-component correlation and obtain competitive compression performance. Even though state-of-the-art color transforms remove some redundancy, they disregard important details of the compression algorithm applied after the transform. Therefore, their coding performance is not optimal. We propose an optimization method called Mosaic Optimization for designing irreversible and reversible color transforms simultaneously optimized for any given WSI and the subsequent compression algorithm. Mosaic Optimization is designed to attain reasonable computational complexity and enable continuous scanner operation. Exhaustive experimental results indicate that, for JPEG 2000 at identical compression ratios, the optimized transforms yield images more similar to the original than other state-of-the-art transforms. Specifically, irreversible optimized transforms outperform the Karhunen-Loève Transform (KLT) in terms of PSNR (up to 1.1 dB), the HDR-VDP-2 visual distortion metric (up to 3.8 dB) and accuracy of computer-aided nuclei detection tasks (F1 score up to 0.04 higher). Additionally, reversible optimized transforms achieve PSNR, HDR-VDP-2 and nuclei detection accuracy gains of up to 0.9 dB, 7.1 dB and 0.025, respectively, when compared to the reversible color transform (RCT) in lossy-to-lossless compression regimes.

Index Terms—Color-Transform Optimization, Whole-Slide Images, Image Compression.

I. INTRODUCTION

In the traditional pathology workflow, pathologists examine specimens under an optical microscope to detect biological structures relevant to the diagnosis. In virtual pathology, traditional glass slides are being replaced by digital *whole-slide images* (WSIs). WSIs allow concurrent examination of a case

This work has been funded by the EU Marie Curie CIG Programme under Grant PIMCO, the Engineering and Physical Sciences Research Council (EPSRC), UK, and by the Spanish Ministry of Economy and Competitiveness and the European Regional Development Fund under Grant TIN2015-71126-R (MINECO/FEDER, UE) and by the Catalan Government under grant 2014SGR-691.

*M. Hernández-Cabronero is with the University of Warwick and the University of Arizona, USA (email: miguelh@email.arizona.edu). Research conducted for this work was performed while M. Hernández-Cabronero was a post-doc at the University of Warwick. V. Sanchez is with the University of Warwick, UK. M. W. Marcellin is with the University of Arizona, USA. F. Aulí-Llinàs, I. Blanes and J. Serra-Sagristà are with the Universitat Autònoma de Barcelona, Spain.

by several pathologists, possibly in different geographical locations, to reduce medical errors [1]. Remote diagnosis can be life-critical in isolated, impoverished or otherwise underserved regions where experts are not available. Moreover, virtual pathology can increase pathologist availability [2] and reduce costs in pathology laboratories [3]. Recently, computer-aided diagnosis (CAD) algorithms are being developed [4]–[12] to assist the pathologists in the diagnosis, especially in tedious and error-prone tasks. WSIs can also enhance performance to help pathologists detect and classify clinical markers, and to create annotated databases for training, research and reference purposes [13].

An important difficulty when dealing with WSIs is their huge size. A 15×15 mm specimen scanned at $40\times$ magnification requires a 60000×60000 , 24-bit RGB color image, resulting in over 10 GB of raw data. Even at a lower, more common $0.5 \mu\text{m}$ resolution, images attain sizes of 30000×30000 and 2.5 GB of uncompressed data [1], [14].

Furthermore, multiple WSIs –sometimes exceeding 35 [15]– are commonly produced per case. Thus, hundreds of Terabytes are produced yearly by a single WSI scanner [15], [16]. These massive data volumes hinder the adoption of virtual pathology. Excessive bandwidth demands can handicap the remote visualization of WSIs, while stringent storage necessities –including archiving and backup systems– can diminish the cost-effectiveness of digital pathology workflows. In such a scenario, image compression is paramount to alleviate these storage and transmission problems.

Lossless coding provides perfect reconstruction of the data produced by the WSI scanner. To the best of our knowledge, only one work has proposed a lossless compression algorithm specific for these images. In [17], High Efficiency Video Coding (HEVC) [18] intra coding mode is adapted to the multidirectional patterns that are typically present in these images. In particular, sample-by-sample differential pulse-code modulation is combined with uniform angular modes to improve prediction across strong edges. However, perfect reconstruction comes at the cost of relatively low compression ratios, commonly between 2:1 and 4:1, which may not suffice for interactive and remote WSI visualization purposes.

On the other hand, lossy compression can offer almost arbitrary ratios at the cost of introducing some distortion in the images. A number of studies –involving pathologists and real specimens– have shown that the images reconstructed with

lossy coding methods are suitable for clinical and research purposes. Compression ratios up to 20:1 with JPEG 2000 [19] yield statistically indistinguishable diagnostic results from those obtained using traditional glass slides [20]–[22], and do not affect the pathologists’ confidence on the diagnosis [23]. Average compression ratios of approximately 13:1 produce images that pathologists deem indiscernible from the original WSIs [24]. Compression ratios up to 200:1 can hinder human-made diagnoses [21], but not some carcinoma-detection CAD algorithms [23]. Traditional JPEG [25] has also been shown to produce reconstructed images that can be employed for diagnosis [26]. Produced results are on par with the ones obtained using glass slides [27], [28], although exact compression ratios for JPEG have not been reported. An accurate rate-allocation method specific for WSIs has also been proposed [29] for lossy regimes with HEVC. In most commercial WSI scanners, standard JPEG 2000 or JPEG compression is employed [14].

Color transforms improve compression by removing inter-component redundancy [30]. Due to the especially strong similarities among color components in WSIs, applying adequate transforms can greatly improve compression performance. WSI-specific color transforms are scarce [31], [32], although other transforms can also be applied to exploit inter-component similarities. In HEVC, fixed color-space translations can be applied to the prediction residuals using the Adaptive Color Transform [33]. JPEG 2000 Part 1 supports the irreversible color transform (ICT) and the reversible color transform (RCT) to decorrelate color components [19]. Arbitrary linear transforms can be used in Part 2 of the standard [34]. In commercial WSI scanners [14] and WSI compression works in the literature [20]–[24], the ICT is the most common color transform. The Karhunen-Loève Transform (KLT) typically produces highly competitive compression results, which normally improve upon the ICT. For Gaussian sources, the KLT is known to provide perfect color component decorrelation. Notwithstanding, WSIs do not follow a Gaussian distribution. Moreover, the KLT does not take into account the details of the compression algorithm applied after the transform. Hence, its compression performance is not optimal either. The Optimal Spectral Transform algorithm (OST [35]) produces linear transforms that minimize the mutual information among color components when they are considered as random variables. Mutual information of two random variables X and Y can be expressed as $I(X; Y) = H(X) - H(X|Y)$, where $H(\cdot)$ denotes the marginal entropy and $H(\cdot|\cdot)$ the conditional entropy. Therefore, lower mutual information implies less redundant information in X and Y , which often improves compression performance. The OST considers the spatial wavelet transform and the quantization of JPEG 2000, but does not consider other important aspects of JPEG 2000 such as its entropy coder. Therefore, its actual compression performance is also suboptimal. Color deconvolution methods are successfully applied in CAD algorithms for WSIs [36]–[38]. These methods separate image colors by using so-called deconvolution matrices, which can be considered color transforms as well. However, these transforms are not designed for compression and do not yield competitive coding performance in practice.

This work introduces a fast mosaic-based optimization

method for designing color transforms that overcomes the inherent drawbacks of the approaches described above. In what follows, this method is referred to as *Mosaic Optimization*. For any input image, Mosaic Optimization produces a color transform that is optimized simultaneously for the image and for the compression algorithm applied after the transform. As a result, the produced transform attains compression performance results that improve upon the state of the art.

To allow reasonable computational complexity, the proposed Mosaic Optimization employs a novel mosaic-based sampling technique. Representative blocks of the image are first extracted using a fast heuristic, and then an optimization process is applied to a mosaic of the extracted blocks. Mosaic Optimization builds upon the *Full Optimization* method, originally presented in [31]. Even though both methods produce transforms that yield very similar compression performance, Full Optimization has a prohibitive computational complexity, i.e., exceeding 2 hours per image on average–, which makes it unusable in practical scenarios. The proposed Mosaic Optimization method enables execution times close to 2.4 minutes on the workstation employed for this research, i.e., 54 times faster than Full Optimization and comparable to the time it takes to scan the WSIs [14], [27]. This allows continuous pipelining of the scanning and the compression of WSIs using reasonable computing power and requiring additional storage space for only one scanned image. Mosaic Optimization also builds upon the *Single Patch Optimization* method introduced in [32]. Although both exhibit similar computational complexity, Mosaic Optimization yields better compression performance than Single Patch Optimization, as discussed later in Section IV. We also propose an extension to design optimized reversible color transforms that can be used for lossless and progressive lossy-to-lossless compression. This can be useful in scenarios where the original data must be stored losslessly, e.g., due to legal restrictions, and bandwidth-efficient lossy representations are necessary, e.g., for remote visualization of the WSIs.

Exhaustive experimental results are provided to evaluate the color transforms produced with Mosaic Optimization when applied to WSIs depicting different tissue types. The PSNR–based on the mean squared error–, the HDR-VDP-2 [39] metric –calibrated to emulate a human observer– and the accuracy of a CAD nuclei detection algorithm [10] are employed for this purpose. Results indicate that the Mosaic Optimization produces irreversible transforms that outperform the ICT and the KLT in terms of PSNR, HDR-VDP-2 and nuclei detection performance. The optimized reversible transforms improve upon the RCT with respect to the PSNR, HDR-VDP-2 and CAD metrics in lossy-to-lossless regimes, i.e., when only part of a losslessly compressed codestream is used for reconstruction. Both the optimized transforms and the RCT produce very similar bitrates in lossless compression regimes.

To recapitulate, we propose a color transform optimization method based on [31]. The main novelties of this work are (a) an original mosaic-based method to reduce computational complexity that outperforms the one described in [32]; (b) an extension of [31] to allow progressive lossy-to-lossless compression; and (c) an exhaustive performance analysis that

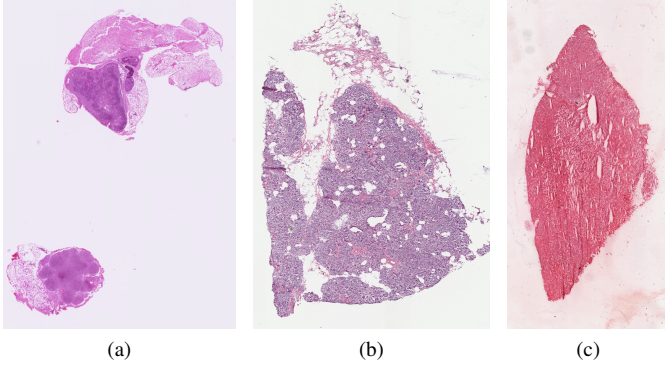


Fig. 1: Sample WSIs depicting (a) lymphatic tissue; (b) pancreatic tissue; (c) renal tissue.

extends those of [31], [32] with more test images, new tissue types and comparison with more color transform design algorithms. With the proposed method, the coding performance of existing compression algorithms can be significantly enhanced and, improving upon [31], only reasonable computational complexity is required. Moreover, the proposed lossy-to-lossless extension broadens the applicability of this work to situations where a lossless copy of the image must be stored.

The rest of the paper is structured as follows. Section II describes key properties of WSIs that motivate the use of color transformations for compression. Section III describes the proposed color-transform optimization framework, including the mosaic-based approach. Section IV provides extensive experimental results and Section V concludes the paper.

II. WHOLE-SLIDE IMAGES AND COLOR TRANSFORMS

A key step to generate WSIs is to stain the biological sample to highlight structures relevant to the diagnostic task at hand. The most commonly employed stain for many types of WSIs is Hematoxylin and Eosin (H&E) [40], which exposes cell nuclei and cytoplasm. The stained slide is then inserted in a special scanner with objective lenses for magnification, which registers a color image depicting the complete glass slide. This takes less than 3 minutes per slide [14], [27].

Optical magnification factors of $20\times$, $40\times$ or even $100\times$ [1], [10], [27] are necessary to provide a microscope-like viewing experience. These magnification factors correspond to resolutions of $0.5\ \mu\text{m}$, $0.25\ \mu\text{m}$ and $0.1\ \mu\text{m}$ per pixel, respectively, and are often used with numerical aperture (NA) of 0.75 [14]. A comprehensive description of the hardware and methods employed to scan WSIs is available in [14]. As a result of the high magnification levels, the 24-bit RGB WSIs output by the scanners have very high spatial resolutions, which motivates compression, but also limits the complexity of the algorithms that can be used under reasonable time and memory constraints.

Due to the staining process, each image exhibits a limited range of color gamut. H&E-stained images typically contain violet, blue and red hues only, as can be seen in Fig. 1. Therefore, WSIs exhibit inter-component redundancy significantly higher than regular photographic imagery. Table I

shows average values if these key characteristics for 50 WSIs considered in this work. In order to provide a meaningful discussion for all types of WSI, a total of 16 types of tissue are hereinafter considered. The average inter-component correlation for these images exceeds 0.95, whereas for the ISO-12640-1 [41] and ISO-12640-2 [42] sets of natural images the average correlation is 0.81 and 0.66, respectively.

Due to the high inter-component correlation present in WSIs, employing adequate color transforms is crucial to obtain competitive compression performance. Traditional static transforms such as YC_bC_r [19] and YIQ [43] translate each RGB pixel into a different color space using a fixed 3×3 matrix $M = (m_{i,j})$:

$$\begin{pmatrix} u \\ v \\ w \end{pmatrix} = \begin{pmatrix} m_{1,1} & m_{1,2} & m_{1,3} \\ m_{2,1} & m_{2,2} & m_{2,3} \\ m_{3,1} & m_{3,2} & m_{3,3} \end{pmatrix} \begin{pmatrix} r \\ g \\ b \end{pmatrix}, \quad (1)$$

where (u, v, w) represents the pixel in the new color space and $m_{i,j}$ are real-valued entries. Typical transforms are not designed for the particular characteristics of WSIs. Thus, they fail to properly decorrelate color components, which in turn may negatively affect compression.

Data-dependent approaches adapt the coefficients of the transform matrix M to the image to be compressed. For instance, the well-known Karhunen-Loève Transform (KLT) removes any inter-component correlation in the transformed image components. Other methods based on independent component analysis such as the Optimal Spectral Transform (OST) [35] minimize the mutual information. In Strutz's work [44], an adaptive transform is implemented by choosing an optimal mode based on the entropy of the image transformed with that mode. Another reversible transform was proposed by Kim et al., which applies an additional lifting step to decorrelate the U and V components produced by the ICT [45]. These data-dependent approaches yield significant compression performance gains as compared to non-adaptive methods. Although data-dependent methods in the literature are designed to optimize criteria such as inter-component correlation or mutual information, none of these methods considers all aspects of the coding algorithm employed after the color transform. For instance, the KLT does not take into account any spatial decorrelation applied after the color transform. The OST includes the 2D discrete wavelet transform (DWT) in its model, but not the probability model used to drive the subsequent entropy coding stage. In turn, Strutz's method evaluates each candidate color transform by applying LOCO-I's [46] spatial predictor after the spectral decorrelation. The entropy of the produced residuals is then used as a surrogate for the actual bitrate of the compressed bitstream. Hence, existing data-dependent color transforms do not attain optimal compression performance either.

III. COLOR TRANSFORM OPTIMIZATION

This section describes a color transform optimization algorithm that attains higher compression efficiency for WSIs than the KLT and other state-of-the-art component transforms. Section III-A describes a numerical transform-optimization framework and Section III-B describes the Mosaic Optimization

TABLE I: Properties of 50 H&E-stained WSIs considered in this work.

Set	#Images	#Tissue Types	Dimensions		Average Inter-Component Correlation			
			Min Size	Max Size	$\rho(R, G)$	$\rho(R, B)$	$\rho(G, B)$	Average
Lymphatic	6	1	12288×17408	17408×25600	0.964	0.976	0.983	0.975
Pancreatic	10	1	12470×12938	31655×32619	0.918	0.919	0.990	0.942
Renal	7	1	9352×8139	34018×16327	0.903	0.908	0.991	0.934
Mixed	27	13	34018×16327	32001×21186	0.955	0.954	0.992	0.967
All images	50	16	9352×8139	31655×32619	0.942	0.943	0.990	0.958

algorithm, which is a fast approximation to this framework. An extension of Mosaic Optimization that allows progressive lossy-to-lossless transmission is introduced in Section III-C.

Note that, even though other parts of the compression pipeline can also be optimized to provide improved compression results [45], the scope of this work is limited to studying and optimizing the color transform stage for WSIs.

A. Optimization Framework

The design of efficient color transforms can be regarded as an optimization problem. For instance, the KLT is defined to remove inter-component correlation, while the OST minimizes inter-component mutual information. These optimization criteria generally have a positive effect on compression, although they are not specifically devised to do so except under certain assumptions such as high-rate scalar quantizers and Gaussian sources for the KLT, which may not hold in practice and therefore lead to suboptimal performance [47]. Contrarily, the proposed framework is conceived to optimize compression performance directly. Given an input image I , our framework aims at finding a transform matrix M that minimizes the cost function EVALUATEDISTORTION,

$$M = \underset{M'}{\operatorname{argmin}} \{ \text{EVALUATEDISTORTION}(M', I) \}. \quad (2)$$

This function appraises a color transform M' by comparing I with the reconstructed image obtained *after compression and decompression* with M' . This scheme is depicted in Fig. 2. Note that, for each I , the same bitrate R must be used for compression in EVALUATEDISTORTION for all color transforms M' so that their relative performance can be compared. A single M that works well for a wide range of R can be obtained by using $R = R_{\text{ICT}}(I)/2$, where $R_{\text{ICT}}(I)$ is the compression rate attained for I by lossy JPEG 2000 using Kakadu v7.8 [48] with its default parameters with the irreversible color transform, without limiting the target bitrate. The value of R for each test image considered in this work is available as supplementary content at <http://ieeexplore.ieee.org>.

By construction, the resulting transform M is not only optimized for I , but also for the compression algorithm employed in the cost function. As discussed in Section I, JPEG 2000 has been successfully employed for compression of WSIs. Part 2 of the standard provides the syntax for user-defined color transforms [34]. Therefore, JPEG 2000 is considered exclusively hereafter. Nevertheless, any other compression algorithm that admits arbitrary linear color transforms could also be used within this framework.

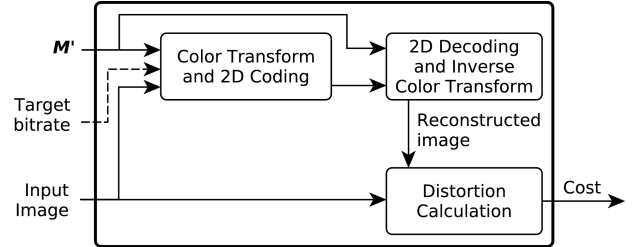


Fig. 2: Diagram of the EVALUATEDISTORTION cost function.

Any distortion metric can be used to compare the input and the reconstructed images in Fig. 2. In this work, the mean squared error (MSE) is employed due to its low computational complexity and its efficient integration with the JPEG 2000 standard. As discussed later in Section IV, optimizing for MSE ultimately improves results for the HDR-VDP-2 metric and for the accuracy of CAD nuclei detection tasks.

Deriving an analytical expression for (2) is not practical for coding systems such as JPEG 2000. This is due to the complex non-linear nature of reversible transforms, spatial decorrelation transforms, quantizers, entropy coders and rate-allocation algorithms. Therefore, unlike for the KLT or the OST, which assume simpler models, closed-form solutions cannot be easily obtained for (2).

To produce competitive transforms, we employ our previously proposed iterative numerical optimization framework, TRANSOPT [31], summarized in Fig. 3. In the Evaluate Candidates box, several candidate transform matrices are compared using the EVALUATEDISTORTION cost function described above. Here, the identity transform (i.e., not applying any color transform), the KLT, the YC_bC_r and the YIQ (a rotation of YC_bC_r) transforms are employed as candidates. Note that the set of initial transforms was empirically chosen to maximize compression performance while minimizing the number of such transforms. Only the best of these, i.e., the one that yields the smallest cost for the input image, is further considered. This transform, denoted “Best candidate M' ” in Fig. 3, undergoes iterative optimization based on Powell’s conjugate direction algorithm [49]. In the i -th iteration of this algorithm, the coefficients of M' are modified using a conjugate gradient method to produce M'_i , to which EVALUATEDISTORTION is applied to obtain Cost_i . Powell’s algorithm employs M'_j and Cost_j , $j \leq i$, to generate M'_{i+1} . This process, depicted with blue dashed arrows in the figure, is repeated N_{iter} times. The output optimized transform M_{opt} is then defined as the M'_i with the smallest associated Cost_i among all iterations. No improvements are observed for $N_{\text{iter}} > 250$.

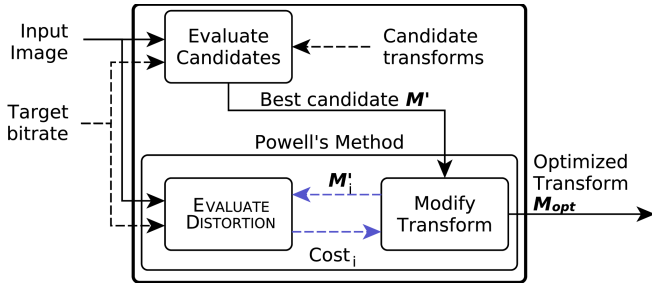


Fig. 3: Diagram of the TRANSOPT transform optimization framework.

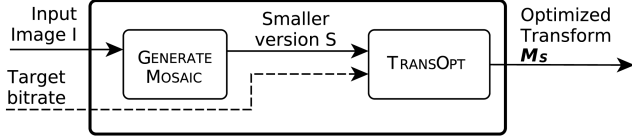


Fig. 4: Diagram of the mosaic-based fast approximation to TRANSOPT.

B. Mosaic Optimization

When the TRANSOPT framework is applied to WSIs, it generates color transforms that improve upon the KLT and other state-of-the-art methods in terms of compression performance. However, this approach—hereafter referred to as *Full Optimization*—exhibits a run time exceeding 130 minutes averaged for the 50 images referenced in Table I, as discussed later in Section IV. A fast mosaic-based approximation to Full Optimization, denoted Mosaic Optimization, is proposed next.

Over 95% of the run time of TRANSOPT is spent in the EVALUATEDISTORTION function in compression, decompression and comparison tasks. To accelerate the execution, a small version S of the input image is generated first, and then the optimization framework is applied to S , as depicted in Fig. 4. It is important to generate a representative version of the full-size image so that the resulting color-transform M_S yields good coding performance for the original image. The proposed method for generating S , referred to as GENERATEMOSAIC, is provided in Algorithm 1. The image is first divided in a rectangular grid with blocks of size $blockSize \times blockSize$ (line 2). Some of the blocks are then selected to build the mosaic image as follows. The number of different pixel colors is computed for each grid block (lines 3–5). Here, a color is defined as the 3D vector (r, g, b) , and two colors (r, g, b) and (r', g', b') are considered identical if and only if $r = r'$, $g = g'$ and $b = b'$. Blocks that contain very few different colors typically depict portions of the background, which is normally bright and homogeneous, as can be observed in Fig. 1. Conversely, blocks with many different colors tend to depict stained tissue and be more representative of the relevant parts of the image. Consistent with this, grid blocks are sorted by the number of colors (line 6) and only the top fraction φ is kept as candidate blocks for the mosaic (line 7), where φ is a real parameter in $(0, 1)$. Finally, blocks are selected with uniform probability from the list of candidates until the total number of pixels reaches a certain target value (line 9).

Algorithm 1 Mosaic-based generation of a smaller image.

```

1: function GENERATEMOSAIC(inputImage, blockSize,  $\varphi$ )
2:   gridBlocks  $\leftarrow$  CREATEGRID(inputImage, blockSize)
3:   for all gridBlocks as block do
4:     block.colors  $\leftarrow$  COUNTDIFFERENTCOLORS(block)
5:   end for
6:   sortedBlocks  $\leftarrow$  SORTBYCOLORS(gridBlocks)
7:   candidateBlocks  $\leftarrow$  sortedBlocks $_{\lfloor sortedBlocks \rfloor \cdot \varphi}$ :
8:     sortedBlocks $_{\lfloor sortedBlocks \rfloor}$ 
9:   selectedBlocks  $\leftarrow$  UNIFORMSAMPLE(candidateBlocks)
10:  mosaicImage  $\leftarrow$  COMBINECELLS(selectedBlocks)
11:  return mosaicImage
12: end function

```

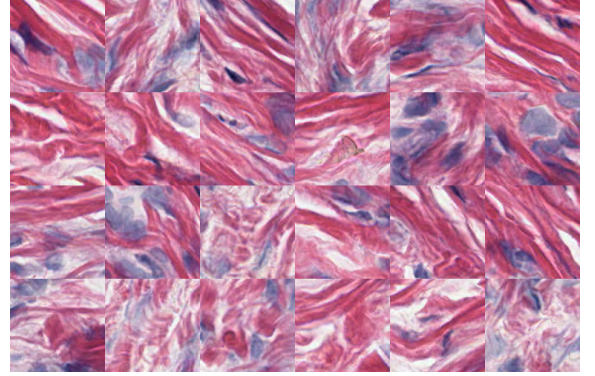


Fig. 5: Crop of a mosaic image produced with Algorithm 1.

For this work, random uniform sampling is used, denoted by UNIFORMSAMPLE in the Algorithm.

The resulting mosaic image is then created by concatenating the selected blocks (line 10), as depicted in Fig. 5. Note that by using adequate values of φ , blocks depicting only background regions, which carry no useful information for the optimization process, are rarely included in the mosaic images.

When the produced mosaic image is used in the EVALUATEDISTORTION function, the JPEG 2000 compressor is invoked with tiles of size $blockSize$, so that the 2D spatial wavelet transform is never performed across the (artificial) block boundaries. Additionally, identical bit budgets are assigned to each mosaic block to avoid individual blocks dominating the rate allocation and the cost function. Since the selected blocks are chosen in a spatially uniform way, the mosaic image is representative of all regions depicting stained tissue. Moreover, the probability of a given biological structure appearing in a block is comparable to the fraction of tissue area depicting this structure. Therefore, this mosaic-based approach produces color transforms M_S optimized to produce good overall performance across the original WSI. This is in contrast with the fast method presented in [32], where the small image version contains pixels from a single area of the image.

The maximum area of the mosaic image, hereinafter referred to as maximum mosaic area (MMA), determines the time complexity of the proposed algorithm. Note that it is the MMA and not φ that has a measurable impact on the size of the produced mosaic images, and therefore on execution times. In general, smaller MMAs need shorter execution times, although

coding performance may be affected when the area is too small. We found that an MMA equal to 0.25% of the original image is adequate to achieve competitive coding performance and computational complexity. This value is employed in the experimental results. Notwithstanding, this parameter can be adjusted to attain faster execution times with a small impact in coding performance. As discussed later in Section IV, using this value results in execution times comparable to the scanning time of many commercial WSI scanners [14], with coding performance similar to Full Optimization. The size of the blocks, determined by *blockSize*, must be selected carefully. Too small blocks yield non-representative performance from JPEG 2000 because of boundary effects at tile edges when the DWT is applied. Too large blocks reduce the number of selected grid blocks, thus limiting the diversity of image regions and features that can be represented in the mosaic image. Block sizes between 128×128 and 256×256 are found to produce the best results.

C. Progressive Lossy-to-Lossless Optimization

The optimized color-transform matrices produced by Mosaic Optimization have real-valued entries. They are irreversible and cannot be directly employed for efficient lossless or progressive lossy-to-lossless compression of WSIs. In some situations it is desirable or even necessary to retain the original image data without loss, e.g., due to archiving policies or legal constraints. Mosaic Optimization can be extended to produce optimized, reversible integer-to-integer color transforms. WSIs can be losslessly compressed with these transforms, achieving compression ratios similar to other state-of-the-art lossless coding algorithms. The losslessly compressed image files can be transmitted partially or progressively, yielding rate-distortion results that improve upon the state of the art.

The proposed extension of the TRANSOPT framework to lossless and lossy-to-lossless scenarios is based on the work by Galli et al. [50]. In that work, transform matrices are factorized as a product of permutation matrices and triangular elementary reversible matrices (TERMs), similar to a well-known lower-upper *LU* matrix decomposition [51], where TERMs are defined as triangular matrices containing only ± 1 in the diagonal. The resulting factorization is equivalent to a reversible integer-to-integer transform that approximates the original lossy transform [50]. In [52], another algorithm for producing reversible transforms based on the matrix factorization proposed in [51] is described. Both [50] and [52] produce accurate approximations. Galli's method is employed exclusively hereafter, and referred to as LOSSLESSAPPROX.

The EVALUATEDISTORTION function is modified to assess the compression performance of the reversible approximation of M' in each iteration of the design procedure. The resulting evaluation function, denoted by REVERSIBLEEVALUATEDISTORTION and depicted in Fig. 6, substitutes EVALUATEDISTORTION in TRANSOPT.

IV. EXPERIMENTAL RESULTS

A. Materials and Methods

To evaluate the performance of the proposed framework, we use 50 H&E images from the Cancer Genome Atlas

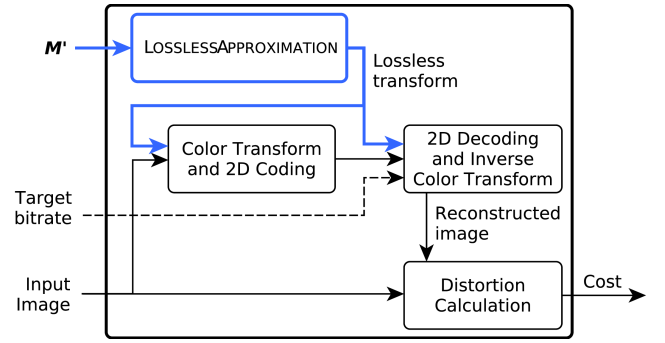


Fig. 6: Diagram of REVERSIBLEEVALUATEDISTORTION.

(TCGA [53]) data portal. Images were selected to depict 16 different tissue types and a broad range of hues so that results can be representative of WSIs in general. The Mosaic Optimization method and its lossy-to-lossless extension are applied to each image to generate optimized irreversible and reversible transforms, respectively. The obtained transform matrices are available as supplementary content at <http://ieeexplore.ieee.org>. The Kakadu v7.8 implementation of JPEG 2000 Part 2 is employed for compression and decompression [48]. In all cases, $N_{iter} = 250$. Our evaluations shown that $blockSize = 128$ and $\varphi = 0.5$ produce the best overall results, hence only these parameters are hereinafter considered. To evaluate complexity, total execution times have been measured on a dedicated workstation with a 4-core i5-4570 CPU at 3.2 GHz and 16 GB of RAM. All reported time results are relative to this platform.

Section IV-B compares Mosaic Optimization to the identity transform (i.e., no color transform), the ICT, the KLT, the OST [35], the YCoCg [54], the color transforms proposed by Strutz et al. [44] and Kim et al. [45], the Full Optimization method described in Section III-A, and the Single Patch Optimization method introduced in [32]. The 50 images summarized in Table I are compressed and reconstructed using each color transform at 15 bitrates ranging from 0.04 to 1.6 bits per pixel per component (bpppc). These correspond to compression ratios from 200:1 to 5:1, typically considered in the literature [20]–[24]. Results for HEVC [18] using the Adaptive Color Transform¹ are also provided for reference.

The optimized reversible transforms are compared in Section IV-C to the default reversible color transform of JPEG 2000 (RCT [19]), the OST [35], the YCoCg-R transform [55], the reversible KLT (RKLT [50]) of each image, and the Single Patch Optimization method. Images are losslessly transformed, compressed and reconstructed at 13 bitrates linearly spaced between 0.04 bpppc and 1.2 bpppc. Five of the 50 images are not included in the comparison since their lossless compression bitrate is lower than 1.2 bpppc. Reversible transforms are not compared to HEVC since it does not provide progressive lossy-to-lossless compression for single images.

Several image distortion metrics have been employed to assess the severity of the distortion introduced in WSIs [23],

¹Produced with the HM reference software v16.5, available at <https://hevc.hhi.fraunhofer.de/>

TABLE II: Average BD*-PSNR and BD*-HDR-VDP-2 results in dB for irreversible color transforms.

Color transform	Lymphatic		Pancreatic		Renal		Mixed		All Images	
	PSNR	VDP								
No transform	42.56	19.13	51.22	38.86	48.31	32.09	47.31	27.07	47.67	29.20
YCoCg	48.33	41.15	51.57	42.06	47.71	30.53	47.82	31.47	48.63	34.93
ICT	47.85	38.72	51.26	42.37	47.01	29.43	47.31	31.38	48.14	34.22
KLT	46.89	38.01	52.38	42.65	48.96	32.45	48.49	30.82	49.14	34.30
OST	46.79	38.82	52.53	41.26	49.50	33.79	47.65	30.78	48.79	34.29
Full Optimization	48.37	42.36	52.70	43.00	49.43	33.41	49.18	31.74	49.83	35.54
Single Patch Optimization	48.02	41.64	50.74	39.69	49.54	32.85	48.56	31.14	49.07	34.37
Mosaic Optimization <i>blockSize</i> = 128, φ = 0.5	48.33	42.82	52.63	43.92	49.27	32.52	49.02	31.77	49.70	35.65

[24], [28], [29], [56]. In [56], the ability of several metrics to detect synthetic noise is evaluated. PSNR is employed in [29] to compare different rate-allocation algorithms for WSIs. In [24], the PSNR, the SSIM and a Visual Discrimination Model (VDM) based on the works by Daly [57] and Lubin [58] are investigated as tools to guide compression of WSIs. In [23], [28], the accuracy of CAD algorithms is employed to evaluate imaging and compression systems, respectively. Consistent with this, the coding performance of the different transforms is appraised using the PSNR, the High Dynamic Range Visual Difference Predictor v2.2.1 [39] (HDR-VDP-2)² and the effect on a recent CAD nuclei detection algorithm [10]. The HDR-VDP-2 metric extends [57] and [58] to predict visible differences between two images, and has been shown [39] to provide higher accuracy than other visual metrics such as SSIM, MS-SSIM [60] and mDCT-PSNR [61].

To compare the average PSNR performance of each transform across all tested bitrates, a modified version of Bjontegaard's BD-PSNR [62] metric is defined as

$$\text{BD}^*\text{-PSNR} = \frac{1}{r_{max} - r_{min}} \int_{r_{min}}^{r_{max}} \text{PSNR}(r) dr. \quad (3)$$

Here, $\text{PSNR}(r)$ is the PSNR between the original and reconstructed image at rate r , and r_{min} and r_{max} are the minimum and maximum reconstruction bitrates. This integral is numerically approximated with Simpson's rule at the aforementioned reconstruction target bitrates. To compare the HDR-VDP-2 metric across the range of tested bitrates, the BD*-HDR-VDP-2 metric is defined analogously. The BD*-PSNR and BD*-HDR-VDP-2 metrics provide, respectively, the average PSNR and HDR-VDP-2 values in dB across the tested bitrate ranges, hence higher values correspond to smaller distortion.

To evaluate the effect of the transforms on the CAD nuclei detection algorithm described in [10], each of the 100 H&E images employed in that study is compressed and reconstructed at the same range of bitrates as described above. The CAD algorithm is then applied to the original and the reconstructed images using the most competitive irreversible and reversible transforms. The nuclei coordinates detected in the original images are used as ground truth and the performance of each transform at each bitrate is calculated

²The probability map produced by the HDR-VDP-2 method is summarized into a single value in dB using the Minkowsky mean as described in [59]. The map is calculated using the default observer model, assuming an RGB display with 100 cd/m² peak luminance, 1 cd/m² black level, and a resolution of 30 pixels per degree.

TABLE III: Average execution times in minutes for obtaining irreversible color transforms.

Algorithm	Lym.	Pan.	Ren.	Mix.	All
KLT	0.2	0.3	0.2	0.3	0.3
OST	19.7	15.1	17.6	19.0	18.0
Full	65.6	113.3	90.5	162.3	130.8
Single Patch	1.2	2.2	1.4	2.7	2.3
Mosaic <i>blockSize</i> = 128, φ = 0.5	1.3	2.5	1.6	2.9	2.4

using the F1 score defined as

$$\text{F1 Score} = \frac{2 \cdot TP}{2 \cdot TP + FP + FN}, \quad (4)$$

where TP (true positives) are the nuclei detected in the original and the reconstructed image, FP (false positives) are the nuclei detected only in the reconstructed image and FN (false negatives) are the nuclei detected in the original image but not in the reconstructed image. F1 scores lie in $[0, 1]$, and higher values indicate better detection performance.

B. Irreversible Transforms

Average BD*-PSNR and BD*-HDR-VDP-2 results for lossy color transforms are provided in Table II for each test set individually³. Consistent with [31], [32], and as expected due to the inter-component correlation described in Table I, all of the transforms (optimized or not) outperform the case of not using any color transform. As can be observed, the ICT – commonly used in WSI scanners [14] and in the WSI compression literature [20]–[24]– yields average BD*-PSNR results 1 dB lower than the KLT, and very similar BD*-HDR-VDP-2 results to the KLT. The YCoCg transform attains similar performance to the ICT, with some improvements in terms of PSNR. In turn, the optimized transforms produced by the Full, Single Patch and Mosaic modes yield average results that are more competitive than the ICT and the KLT. In particular, Full Optimization and Mosaic Optimization improve upon the ICT and the KLT for each set and for both distortion metrics. Average results for the OST are slightly lower than those of the KLT in terms of PSNR, and very similar in terms of the HDR-VDP-2 metric.

³BD*-PSNR and BD*-HDR-VDP-2 results for HEVC are not included in Table II because the maximum bitrates are below 1 bpppc for most images, even for the lowest QP value of 1. Hence, a fair comparison for rates $r \in [r_{min}, r_{max}]$ is not possible. Results for HEVC are included in Figs. 7a and 7b.

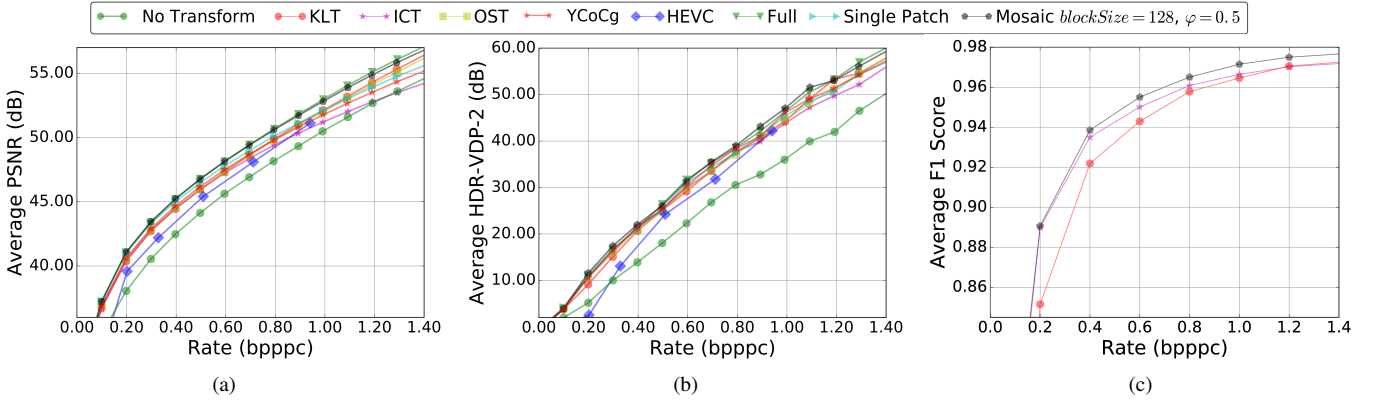


Fig. 7: Average rate-distortion comparison of irreversible transforms for all images (a) using the PSNR metric; (b) using the HDR-VDP-2 metric; (c) using the F1 score based on [10].

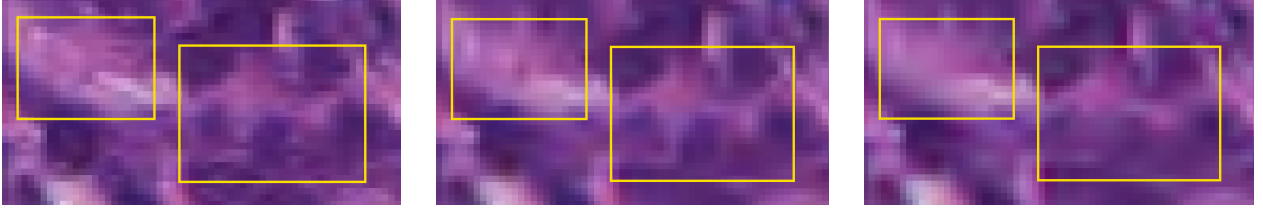


Fig. 8: Magnified sample crop (50×90) of image *NCI02* of the Lymphatic set. (left) Original; (center) reconstructed at 0.1 bpppc using Mosaic Optimization; (right) reconstructed at 0.1 bpppc using the KLT. Areas of interest are highlighted in yellow.

Full Optimization yields better BD^* -PSNR results than Mosaic Optimization for all test sets. This is because all image samples are available for optimization in the Full mode. Notwithstanding, Mosaic Optimization provides very similar results for each set, between 0.04 dB and 0.16 dB lower than the Full mode. In terms of BD^* -HDR-VDP-2, Mosaic Optimization exhibits gains over Full Optimization of up to 0.92 dB for the Pancreatic set, and 0.11 dB on average for all images. This can be explained by the fact that Mosaic Optimization prioritizes candidate grid blocks depicting tissue. Hence, the resulting color transforms enable more accurate reconstruction of visually relevant areas, e.g., edges between nuclei and cytoplasm.

Average PSNR and HDR-VDP-2 rate-distortion results are plotted in Figs. 7a and 7b, respectively. Results indicate that PSNR gains between 0.6 dB and 1.1 dB and HDR-VDP-2 gains up to 3.8 dB over the KLT are obtained with the proposed method at the same bitrates. Therefore, at identical compressed file sizes, images reconstructed using the Mosaic Optimization method exhibit smaller distortion –e.g., fewer morphological and chromatic artifacts– than those reconstructed using the KLT, as illustrated in Fig. 8. Note that a low bitrate (0.1 bpppc) is used in Fig. 8 so that artifacts are more easily appreciable. These artifacts disappear at higher bitrates. Mosaic Optimization attains similar PSNR and HDR-VDP-2 levels –i.e., similar quality– at bitrates between 0.05 bpppc and 0.10 bpppc lower than the KLT, i.e., smaller compressed files. Thus, the transmission of images at similar quality levels can be completed faster. For instance, PSNR values of approximately 47 dB are produced on average at 0.5 bpppc for the optimized transforms and at 0.6 bpppc for the KLT,

i.e., 20% data volume reduction. As can also be observed in Figs. 7a and 7b, the proposed method is better than HEVC with the Adaptive Color Transform for the PSNR and HDR-VDP-2 metrics.

Average F1 scores for the KLT, for the ICT and for Mosaic Optimization obtained for the CAD nuclei detection algorithm described in [10] are plotted in Fig. 7c. As can be observed, all transforms produce F1 scores above 0.9 at bitrates as low as 0.4 bpppc. Mosaic Optimization produces F1 scores consistently higher than the ICT and the KLT for all tested bitrates. These results suggest that, for any compression ratio, the Mosaic Optimization method enables more accurate CAD analysis results than the ICT and the KLT.

Average execution times for obtaining different data-dependent irreversible color transforms are provided in Table III. Note that these times refer to the time it takes to generate the color transform matrices, not the time it takes to compress an image using that transform matrix. For all tested image sets, the KLT is the fastest algorithm. However, as discussed above, its coding performance is lower than that of the optimization methods. Full Optimization has an average execution time exceeding 130 minutes, rendering it impractical for most use cases. On the other hand, Mosaic Optimization requires under 2 minutes for the Lymphatic and Renal image sets, and under 3 minutes for the Pancreatic and Mixed sets. These execution times are comparable to the scanning time of many commercial scanners, i.e., up to 3 minutes depending on the objective magnification [14], [27].

To recapitulate, the optimized transforms produced by the proposed method outperform the ICT –the most usual transform in commercial scanners and in the WSI compression

TABLE IV: Average BD*-PSNR and BD*-HDR-VDP-2 results in dB for reversible color transforms.

Color transform	Lymphatic		Pancreatic		Renal		Mixed		All Images	
	PSNR	VDP								
No Transform	35.37	11.83	44.07	18.48	41.03	12.28	41.21	12.95	40.59	13.84
RCT	42.87	18.64	45.43	20.04	41.13	13.13	42.26	15.34	42.82	16.85
YCoCg-R	39.88	12.02	42.25	18.13	41.10	12.83	41.77	12.56	41.79	13.74
Strutz's [44]	42.91	18.97	45.46	20.05	41.15	13.17	42.44	15.48	42.87	16.93
Kim's [45]	41.56	11.82	42.12	18.61	41.38	12.72	41.70	12.65	42.51	13.79
OST	41.58	20.08	44.84	19.15	41.69	13.21	42.28	14.53	42.62	16.15
RKLT	42.06	21.19	44.84	18.71	41.35	13.04	42.43	15.62	42.72	16.64
Single Patch Optimization	42.88	22.29	45.37	20.12	41.75	13.26	42.91	15.13	43.24	17.36
Mosaic Optimization <i>blockSize</i> = 128, φ = 0.5	43.11	25.07	45.47	21.09	41.76	13.33	42.86	15.51	43.27	17.61

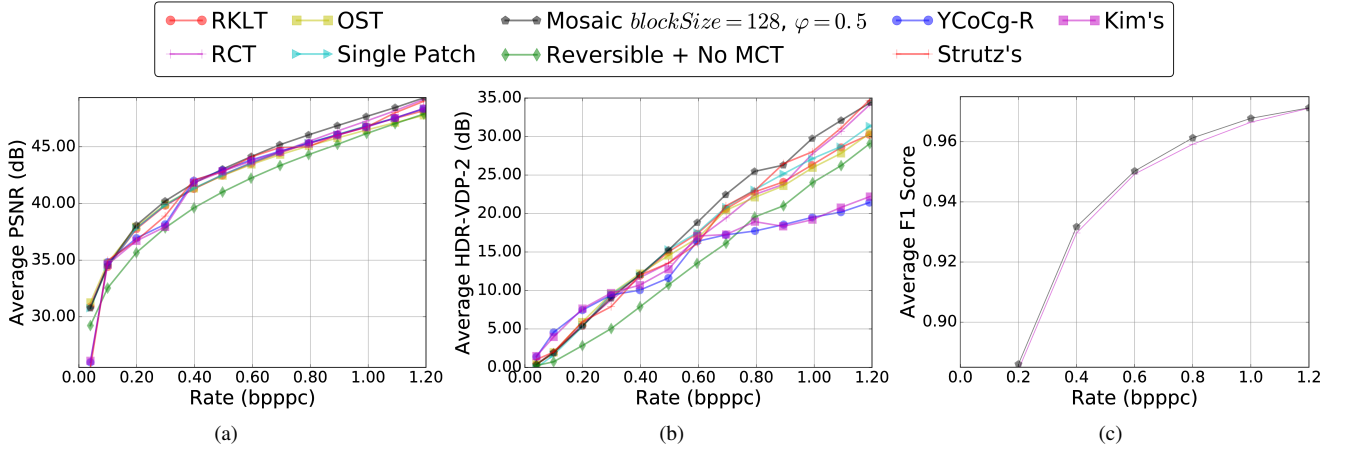


Fig. 9: Average rate-distortion comparison of reversible transforms for all images (a) using the PSNR metric; (b) using the HDR-VDP-2 metric; (c) using the F1 score based on [10].

literature— as well as transforms such as the KLT and the OST for traditional, visual and CAD-based distortion metrics.

C. Reversible Transforms

Average BD*-PSNR and BD*-HDR-VDP-2 results for the reversible transforms are provided in Table IV. As can be observed, the proposed Mosaic Optimization method improves upon the RCT, the OST, Single Patch and the RKT in almost all cases. In general, larger improvements are observed for the BD*-HDR-VDP-2 than for the BD*-PSNR metrics. Again, this is explained by the fact that optimization is designed to focus on visually relevant areas of the WSIs. Note that the compression performance differences between the irreversible transforms described in Section IV-B can be largely explained by the different DWTs used for 2D decorrelation, i.e., the CDF 9/7 DWT for irreversible transforms and the integer-to-integer CDF 5/3 DWT for reversible ones.

As shown in Figs. 9a and 9b, significant PSNR improvements over the RKT are observed for bitrates of 0.2 bpppc and higher, with gains up to 0.9 dB. HDR-VDP-2 improvements become significant from 0.4 bpppc onwards, with maximum gains of 3.7 dB. Results suggest that similar distortion can be attained for smaller data volumes with the proposed method, e.g., an average PSNR of 44 dB can be obtained transmitting 14% less data. Note that bitrates of 0.4 bpppc (i.e., compression ratios of 20:1) are often described in the WSI compression literature [21]–[24] and a average bitrates of

about 0.6 bpppc (i.e., a compression ratio of about 13:1) have been described to produce reconstructed images indiscernible from the original [24]. These ranges are well aligned with the bitrate ranges for which the proposed Mosaic method yields compression gains.

Lossless compression bitrates are provided in Table V. On average for all images, all tested methods yield similar results. This indicates that the progressive lossy-to-lossless coding gains produced by the Mosaic Optimization method are not at the expense of hindering lossless compression efficiency, as compared to other works in the literature.

Average F1 scores for the RCT and for Mosaic Optimization obtained for the CAD nuclei detection algorithm described in [10] are plotted in Fig. 9c. As can be observed, both the RCT and Mosaic Optimization allow accurate CAD-based analysis of the images, with F1 scores above 0.9 for bitrates of 0.27 bpppc or higher. Identical F1 scores can be obtained at bitrates up to 0.1 bpppc lower with Mosaic Optimization than with the RCT.

Average execution times for producing reversible transforms using different methods are shown in Table VI. Note that compression time is not included in this table. As can be observed, generating the reversible optimized transforms requires about 19 minutes on average for all images. The higher time complexity, compared to the irreversible transform optimization methods discussed in the previous section is expected, due to the additional approximation stage required in each invocation of the REVERSIBLEEVALUATEDISTORTION

TABLE V: Average lossless compression rates in bpppc.

Color transform	Lym.	Pan.	Ren.	Mix.	All
No Transform	3.41	1.98	1.96	2.07	2.14
RCT	2.44	1.90	1.98	1.97	2.00
YCoCg-R	2.36	1.87	1.99	2.02	1.99
Strutz's [44]	2.35	1.86	1.94	1.99	1.96
Kim's [45]	2.42	1.84	2.01	2.03	1.99
OST	2.96	2.01	1.99	2.06	2.15
RKLT	2.87	2.09	1.99	1.94	2.09
Single Patch	2.71	2.01	1.93	1.95	2.02
Mosaic $blockSize = 128,$ $\varphi = 0.5$	2.69	1.96	1.87	1.92	1.99

TABLE VI: Average execution times in minutes for obtaining reversible color transforms.

Algorithm	Lym.	Pan.	Ren.	Mix.	All
RKLT	0.44	0.52	0.41	0.49	0.47
OST	19.94	15.33	17.84	19.21	18.48
Strutz's [44]	0.65	1.74	0.81	1.58	1.39
Kim's [45]	0.51	1.20	0.54	1.14	0.99
Single Patch	8.74	23.64	10.50	22.61	19.46
Mosaic $blockSize = 128$ $\varphi = 0.5$	9.40	21.26	10.91	22.72	19.18

function, depicted in Fig. 6.

V. CONCLUSIONS

WSIs can help pathologists improve their diagnostic accuracy, reach underserved regions and enhance their productivity, thus reducing the operational costs of pathology laboratories. However, the enormous data volumes associated with WSIs make image compression necessary to enable efficient storage and agile remote access. In particular, lossy compression can greatly reduce compressed data volumes without affecting pathologists' diagnoses or their confidence therein. WSIs exhibit exceptionally high inter-component correlation, which can be exploited using color transforms that enhance coding performance. Color transforms in the literature are designed to minimize theoretical criteria such as correlation, but do not fully take into account all details of the coding algorithm applied after the transform. Therefore, in practice, their compression performance is suboptimal. The proposed Mosaic Optimization method is tightly integrated with the implementation of the coding algorithm used in the Kakadu implementation and the produced color transforms improve upon the ICT, the KLT and other methods in terms of mean squared error (PSNR), visual distortion metrics (HDR-VDP-2) and F1 score for a recent CAD nuclei detection algorithm. At identical rates, PSNR values up to 1.1 dB higher, HDR-VDP-2 results up to 3.8 dB higher and average F1 scores up to 0.04 higher than the KLT are obtained. Conversely, equal distortion levels are produced for bitrates between 0.05 bpppc and 0.17 bpppc lower, i.e., file sizes up to 20% smaller than for the KLT. An extension to design reversible transforms is proposed as well to allow lossless and progressive lossy-to-lossless compression. Without hindering lossless compression performance, the optimized transforms yield average PSNR values up to 0.9 dB higher, average HDR-VDP-2 results up to 7.1 dB higher, and average F1

scores 0.025 higher than the RCT at the same bitrates. Similar distortion levels are obtained at bitrates up to 14% lower than for the RCT. Moreover, Mosaic Optimization is designed to attain execution times comparable to that of a typical WSI scanning process. This enables continuous operation of the WSI scanner with only reasonable computational resources dedicated to compression. In summary, the proposed color-transform optimization method can produce tangible benefits for WSI-centered laboratories in practical scenarios.

ACKNOWLEDGMENTS

We thank M. Barret for kindly providing an implementation of the OST algorithm from [35], and the authors of [10] for sharing an implementation of their CAD nuclei detection algorithm.

REFERENCES

- [1] M. May, "A better lens on disease," *Scientific American*, vol. 302, no. 5, pp. 74–7, May 2010.
- [2] J. Ho, S. M. Ahlers, C. Stratman, O. Aridor, L. Pantanowitz, J. L. Fine, J. A. Kuzmishin, M. C. Montalto, and A. V. Parwani, "Can digital pathology result in cost savings? A financial projection for digital pathology implementation at a large integrated health care organization," *Journal of Pathology Informatics*, vol. 5, no. 33, 2014.
- [3] M. Isaacs, J. K. Lennerz, S. Yates, W. Clermont, J. Rossi, and J. D. Pfeifer, "Implementation of whole slide imaging in surgical pathology: A value added approach," *Journal of Pathology Informatics*, vol. 2, no. 39, 2011.
- [4] A. Madabhushi, "Digital pathology image analysis: opportunities and challenges," *Imaging in Medicine*, vol. 1, no. 1, pp. 7–10, 2009.
- [5] O. Sertel, J. Kong, H. Shimada, U. V. Catalyurek, J. H. Saltz, and M. N. Gurcan, "Computer-aided Prognosis of Neuroblastoma on Whole-slide Images: Classification of Stromal Development," *Pattern recognition*, vol. 42, no. 6, pp. 1093–1103, Jun. 2009.
- [6] M. D. DiFranco, G. O'Hurley, E. W. Kay, R. W. G. Watson, and P. Cunningham, "Ensemble based system for whole-slide prostate cancer probability mapping using color texture features," *Computerized Medical Imaging and Graphics*, vol. 35, no. 7–8, pp. 629–45, Jan. 2011.
- [7] S. Samsi, A. K. Krishnamurthy, and M. N. Gurcan, "An efficient computational framework for the analysis of whole slide images: Application to follicular lymphoma immunohistochemistry," *Journal of Computational Science*, vol. 3, no. 5, pp. 269–279, Sep. 2012.
- [8] J. Xu, L. Xiang, Q. Liu, H. Gilmore, J. Wu, J. Tang, and A. Madabhushi, "Stacked Sparse Autoencoder (SSAE) for Nuclei Detection on Breast Cancer Histopathology Images," *IEEE Trans. Med. Imag.*, vol. 35, no. 1, pp. 119–130, Jan. 2016.
- [9] S. B. Ginsburg, G. Lee, S. Ali, and A. Madabhushi, "Feature Importance in Nonlinear Embeddings (FINE): Applications in Digital Pathology," *IEEE Trans. Med. Imag.*, vol. 35, no. 1, pp. 76–88, Jan. 2016.
- [10] K. Sirinukunwattana, S. E. A. Raza, Y. W. Tsang, D. R. J. Snead, I. A. Cree, and N. M. Rajpoot, "Locality Sensitive Deep Learning for Detection and Classification of Nuclei in Routine Colon Cancer Histology Images," *IEEE Trans. Med. Imag.*, vol. 35, no. 5, pp. 1196–1206, May 2016.
- [11] A. Vahadane, T. Peng, A. Sethi, S. Albarqouni, L. Wang, M. Baust, K. Steiger, A. M. Schlitter, I. Esposito, and N. Navab, "Structure-Preserving Color Normalization and Sparse Stain Separation for Histological Images," *IEEE Trans. Med. Imag.*, vol. 35, no. 8, pp. 1962–1971, Aug. 2016.
- [12] B. E. Bejnordi, M. Balkenhol, G. Litjens, R. Holland, P. Bult, N. Karssemeijer, and J. A. W. M. van der Laak, "Automated Detection of DCIS in Whole-Slide H&E Stained Breast Histopathology Images," *IEEE Trans. Med. Imag.*, vol. 35, no. 9, pp. 2141–2150, Sep. 2016.
- [13] The Digital Pathology Association. (2017) Whole Slide Imaging Repository. [Online]. Available: <https://digitalpathologyassociation.org/whole-slide-imaging-repository>
- [14] N. Farahani, A. Parwani, and L. Pantanowitz, "Whole slide imaging in pathology: advantages, limitations, and emerging perspectives," *Pathology and Laboratory Medicine International*, vol. Volume 7, p. 23, Jun. 2015.

- [15] D. R. J. Snead, Y.-W. Tsang, A. Meskiri, P. K. Kimani, R. Crossman, N. M. Rajpoot, E. Blessing, K. Chen, K. Gopalakrishnan, P. Matthews, N. Momtahan, S. Read-Jones, S. Sah, E. Simmons, B. Sinha, S. Suortamo, Y. Yeo, H. El Daly, and I. A. Cree, "Validation of digital pathology imaging for primary histopathological diagnosis," *Histopathology*, vol. 68, no. 7, pp. 1063–1072, 2016.
- [16] A. Huisman, A. Looijen, S. M. van den Brink, and P. J. van Diest, "Creation of a fully digital pathology slide archive by high-volume tissue slide scanning," *Human pathology*, vol. 41, no. 5, pp. 751–757, 2010.
- [17] V. Sanchez, F. Auli-Llinàs, J. Bartrina-Rapesta, and J. Serra-Sagrà, "HEVC-based Lossless Compression of Whole Slide Pathology Images," in *IEEE Conference on Signal and Information Processing (GlobalSIP)*. IEEE, Dec. 2014, pp. 297–301.
- [18] G. J. Sullivan, J. R. Ohm, W. J. Han, and T. Wiegand, "Overview of the High Efficiency Video Coding (HEVC) Standard," *IEEE Trans. Circuits Syst. Video Technol.*, vol. 22, no. 12, pp. 1649–1668, Dec. 2012.
- [19] D. S. Taubman and M. W. Marcellin, *JPEG 2000: Image Compression Fundamentals, Standards and Practice*. Kluwer Academic Publishers, Nov. 2001.
- [20] T. Kalinski, R. Zwönitzer, S. Sel, M. Evert, T. Guenther, H. Hofmann, J. Bernarding, and A. Roessner, "Virtual 3D Microscopy Using Multi-plane Whole Slide Images in Diagnostic Pathology," *American Journal of Clinical Pathology*, vol. 130, no. 2, pp. 259–264, 2008.
- [21] T. Kalinski, R. Zwönitzer, F. Grabellus, S. Y. Sheu, S. Sel, H. Hofmann, J. Bernarding, and A. Roessner, "Lossy compression in diagnostic virtual 3-dimensional microscopy – where is the limit?" *Human Pathology*, vol. 40, no. 7, pp. 998–1005, 2009.
- [22] T. Kalinski, R. Zwönitzer, F. Grabellus, S. Y. Sheu, S. Sel, H. Hofmann, and A. Roessner, "Lossless compression of JPEG2000 whole slide images is not required for diagnostic virtual microscopy," *American Journal of Clinical Pathology*, vol. 136, no. 6, pp. 889–895, 2011.
- [23] S. Doyle, J. Monaco, A. Madabhushi, S. Lindholm, P. Ljung, L. Ladic, J. Tomaszewski, and M. Feldman, "Evaluation of effects of JPEG2000 compression on a computer-aided detection system for prostate cancer on digitized histopathology," in *IEEE International Symposium on Biomedical Imaging: From Nano to Macro (ISBI)*, Apr. 2010, pp. 1313–1316.
- [24] J. P. Johnson, E. A. Krupinski, M. Yan, H. Roehrig, A. R. Graham, and R. S. Weinstein, "Using a visual discrimination model for the detection of compression artifacts in virtual pathology images," *IEEE Trans. Med. Imag.*, vol. 30, no. 2, pp. 306–14, Feb. 2011.
- [25] *JPEG Requirements and guidelines*, ISO/IEC IS Std. 10918-1, 1994.
- [26] A. Sharma, P. Bautista, and Y. Yagi, "Balancing image quality and compression factor for special stains whole slide images," *Analytical Cellular Pathology*, vol. 35, no. 2, pp. 101–106, 2012.
- [27] D. D. Rhoads, N. F. Habib-Bein, R. S. Hariri, D. J. Hartman, S. E. Monaco, A. Lesniak, J. Duboy, M. E.-S. Salama, and L. Pantanowitz, "Comparison of the diagnostic utility of digital pathology systems for telemicrobiology," *Journal of Pathology Informatics*, vol. 7, p. 10, 2016.
- [28] L. Barisoni, J. P. Troost, C. Nast *et al.*, "Reproducibility of the NEPTUNE descriptor-based scoring system on whole-slide images and histologic and ultrastructural digital images," *Modern Pathology*, vol. 29, no. 7, pp. 671–684, Jul. 2016.
- [29] V. Sanchez, F. Auli-Llinàs, R. Vanam, and J. Bartrina-Rapesta, "Rate control for lossless region of interest coding in HEVC intra-coding with applications to digital pathology images," in *IEEE International Conference on Acoustics, Speech and Signal Processing (ICASSP)*, Apr. 2015, pp. 1250–1254.
- [30] V. Goyal, "Theoretical foundations of transform coding," *IEEE Trans. Signal Process.*, vol. 18, no. 5, pp. 9–21, 2001.
- [31] M. Hernández-Cabrero, F. Auli-Llinàs, V. Sanchez, and J. Serra-Sagrà, "Transform Optimization for the Lossy Coding of Pathology Whole-Slide Images," in *Proceedings of the Data Compression Conference, DCC*, Mar. 2016.
- [32] M. Hernández-Cabrero, V. Sanchez, F. Auli-Llinàs, and J. Serra-Sagrà, "Fast MCT Optimization for the Compression of Whole-Slide Images," in *Proceedings of the IEEE International Conference on Image Processing, ICIP*, Sep. 2016, pp. 2370–2374.
- [33] L. Zhang, J. Chen, J. Sole, M. Karczewicz, X. Xiu, and J. Z. Xu, "Adaptive Color-Space Transform for HEVC Screen Content Coding," in *Proceedings of the Data Compression Conference, DCC*, April 2015, pp. 233–242.
- [34] *JPEG 2000 image coding system: Core coding system*, ISO/IEC IS Std. 15444-2, 2004.
- [35] I. P. Akam Bitá, M. Barret, and D. T. Pham, "On optimal transforms in lossy compression of multicomponent images with JPEG2000," *Signal Processing*, vol. 90, no. 3, pp. 759–773, 2010.
- [36] A. C. Ruifrok and D. A. Johnston, "Quantification of histochemical staining by color deconvolution," *Analytical and quantitative cytology and histology*, vol. 23, no. 4, pp. 291–299, 2001.
- [37] M. K. K. Niazi, K. Yao, D. Zynger, S. Clinton, J. Chen, M. Koyuturk, T. LaFramboise, and M. Gurcan, "Visually meaningful histopathological features for automatic grading of prostate cancer," *IEEE Journal of Biomedical and Health Informatics*, 2016, In press.
- [38] M. K. K. Niazi, A. V. Parwani, and M. N. Gurcan, "Computer-assisted bladder cancer grading: α -shapes for color space decomposition," in *SPIE Medical Imaging*, 2016, pp. 979 107–1 – 979 107–8.
- [39] R. Mantiuk, K. J. Kim, A. G. Rempel, and W. Heidrich, "HDR-VDP-2: a calibrated visual metric for visibility and quality predictions in all luminance conditions," in *ACM Transactions on Graphics (TOG)*, vol. 30, no. 4. ACM, 2011, p. 40.
- [40] A. Khan, N. Rajpoot, D. Treanor, and D. Magee, "A Non-Linear Mapping Approach to Stain Normalisation in Digital Histopathology Images using Image-Specific Colour Deconvolution," *IEEE Trans. Biomed. Eng.*, vol. 61, no. 6, pp. 1729–1738, 2014.
- [41] *Graphic technology - Prepress digital data exchange - Part 1: CMYK standard colour image data*, International Standard Organization (ISO) Std. 12640-1, 1997. [Online]. Available: http://www.iso.org/iso/catalogue_detail.htm?csnumber=40928
- [42] *Graphic technology - Prepress digital data exchange - Part 2: RGB encoded standard colour image data*, International Standard Organization (ISO) Std. 12640-2, 2004.
- [43] W. H. Buchsbaum, *Color TV Servicing*, E. Cliffs, Ed. Prentice Hall, 1975.
- [44] T. Strutz, "Multiplierless reversible color transforms and their automatic selection for image data compression," *IEEE Trans. Circuits Syst. Video Technol.*, vol. 23, no. 7, pp. 1249–1259, Jul. 2013.
- [45] S. Kim and N. I. Cho, "Hierarchical prediction and context adaptive coding for lossless color image compression," *IEEE Trans. Image Process.*, vol. 23, no. 1, pp. 445–449, Jan 2014.
- [46] M. J. Weinberger, G. Seroussi, and G. Sapiro, "The loco-i lossless image compression algorithm: Principles and standardization into jpegs," *IEEE Transactions on Image processing*, vol. 9, no. 8, pp. 1309–1324, 2000.
- [47] M. Effros, H. Feng, and K. Zeger, "Suboptimality of the Karhunen-Loeve transform for transform coding," *IEEE Trans. Inf. Theory*, vol. 50, no. 8, pp. 1605–1619, Aug 2004.
- [48] Kakadu JPEG2000 implementation, available [Online]: <http://www.kakadusoftware.com>, 2017.
- [49] J. Nocedal and S. Wright, *Numerical Optimization*. Springer, 2006.
- [50] L. Galli and S. Salzo, "Lossless hyperspectral compression using KLT," in *IEEE International Geoscience and Remote Sensing Symposium, IGRSS*, vol. 1, Sep. 2004, p. 316.
- [51] P. Hao and Q. Shi, "Matrix factorizations for reversible integer mapping," *IEEE Trans. Signal Process.*, vol. 49, no. 10, pp. 2314–2324, Oct. 2001.
- [52] S. C. Pei and J. J. Ding, "Improved reversible integer-to-integer color transforms," in *Proceedings of the IEEE International Conference on Image Processing, ICIP*, Nov. 2009, pp. 473–476.
- [53] "The Cancer Genome Atlas, National Cancer Institute, National Institute of Health," Available [Online]: <https://cancergenome.nih.gov/>.
- [54] H. Malvar and G. Sullivan, "Transform, scaling & color space impact of professional extensions," *ISO/IEC JTC1/SC29/WG11 and ITU-T SG16 Q*, vol. 6, 2003.
- [55] S. S. Henrique S. Malvar, Gary J. Sullivan, "Lifting-based reversible color transformations for image compression," pp. 7073.1 – 7073.10, 2008.
- [56] A. Jiménez, G. Bueno, G. Cristóbal, O. Déniz, D. Toomey, and C. Conway, "Image quality metrics applied to digital pathology," *SPIE Photonics Europe*, vol. 9896, p. 98960S, 2016.
- [57] S. Daly, *Digital Images and Human Vision*. MIT Press, 1993, ch. The Visible Differences Predictor: An Algorithm for the Assessment of Image Fidelity, pp. 179–206.
- [58] J. Lubin, *Vision Models for Target Detection and Recognition*. World Scientific, 1995, vol. 2, ch. A visual discrimination model for imaging system design and evaluation, pp. 245–357.
- [59] K. J. Kim, B. Kim, R. Mantiuk, T. Richter, H. Lee, H. S. Kang, J. Seo, and K. H. Lee, "A Comparison of Three Image Fidelity Metrics of Different Computational Principles for JPEG2000 Compressed Abdomen CT Images," *IEEE Trans. Med. Imag.*, vol. 29, no. 8, pp. 1496–1503, Aug. 2010.
- [60] Z. Wang, E. P. Simoncelli, and A. C. Bovik, "Multiscale structural similarity for image quality assessment," in *Asilomar Conference on Signals, Systems and Computers*, vol. 2, Nov. 2003, pp. 1398–1402.

- [61] T. Richter, "On the mDCT-PSNR image quality index," in *International Workshop on Quality of Multimedia Experience (QoMEx)*, Jul. 2009, pp. 53–58.
- [62] G. Bjontegaard, "Calculation of average PSNR differences between RD-curves," Tech. Rep. VCEG-M33 ITU-T Q6/16, Apr. 2001.